CORA Cork Open Research Archive
Cartlann Taighde Oscailte Chorcaí

Title	The effect of particle size, morphology and C-rates on 3D structured Co 3 O 4 inverse opal conversion mode anode materials
Authors	McNulty, David;Geaney, Hugh;Carroll, Elaine;Garvey, Shane;Lonergan, Alex;O'Dwyer, Colm
Publication date	2017-02-01
Original Citation	David, M., Hugh, G., Elaine, C., Shane, G., Alex, L. and Colm, O. D. (2017) 'The effect of particle size, morphology and C-rates on 3D structured Co 3 O 4 inverse opal conversion mode anode materials', Materials Research Express, 4(2), 025011 (11pp). doi: 10.1088/2053-1591/aa5a26
Type of publication	Article (peer-reviewed)
Link to publisher's version	http://iopscience.iop.org/article/10.1088/2053-1591/aa5a26/pdf - 10.1088/2053-1591/aa5a26
Rights	© 2017 IOP Publishing Ltd. This is an author-created, un-copyedited version of an article accepted for publication in Materials Research Express. The publisher is not responsible for any errors or omissions in this version of the manuscript or any version derived from it. The Version of Record is available online at https://doi.org/10.1088/2053-1591/aa5a26
Download date	2026-11-03 15:25:21
Item downloaded from	https://hdl.handle.net/10468/6128

UCC
University College Cork, Ireland
Coláiste na hOllscoile Corcaigh

The Effect of Particle Size, Morphology and C-rates on 3D Structured Co_3O_4 Inverse Opal Conversion Mode Anode Materials

David McNulty [1,2], **Hugh Geaney** [1,2], **Elaine Carroll** [1,2], **Shane Garvey** [1], **Alex Lonergan** [1],

and **Colm O'Dwyer** [1,2,3*]

[1] *Department of Chemistry, University College Cork, Cork T12 YN60, Ireland*
[2] *Tyndall National Institute, Lee Maltings, Cork T12 R5CP, Ireland*
[3] *Micro-Nano Systems Centre, Tyndall National Institute, Lee Maltings, Cork T12 R5CP, Ireland*

*****Corresponding author: Tel: +353 (0)21 4902732; Fax: +353 (0)21 4274097; email: c.odwyer@ucc.ie

Abstract

Engineering Co_3O_4 nanoparticles into highly ordered, 3D inverse opal (IO) structures is shown to significantly improve their performance as more efficient conversion mode Li-ion anode materials. By comparison with Co_3O_4 microparticles, the advantages of the porous anode architecture are clearly shown. The inverse opal material markedly enhances specific capacity and capacity retention. The impact of various C rates on the rate of the initial charge demonstrates that higher rate charging (10 C) was much less destructive to the inverse opal structure than charging at a slow rate (0.1 C). Slower C rates that affect the IO structure resulted in higher specific capacities (more Li_2O) as well as improved capacity retention. The IO structures cycle as CoO, which improves Coulombic efficiency and limits volumetric changes, allowing rate changes more efficiently. This work demonstrates how 3D IOs improve conversion mode anode material performance in the absence of additive or binders, thus enhancing mass transport of Li_2O charge-discharge product through the open structure. This effect mitigates clogging by structural changes at slow rates (high capacity) and is beneficial to the overall electrochemical performance.

1. Introduction

The development of anode materials for Li-ion applications has attracted significant research attention aimed at improving the performance over commercially utilized graphite. [1-4] Unlike conventional carbon based anode materials, transition metal oxides (TMOs) that react with Li through conversion reactions offer great potential for enhanced performance due to the differences in their lithiation mechanisms. [5-7] Rather than operating *via* a standard intercalation process, conversion mode materials undergo reversible redox reactions during charging and discharging. These reactions typically involve a higher mole fraction of Li per unit material (compared to intercalation) and, as a result, conversion mode materials can possess higher theoretical specific energies. [5, 8-10] To date, extensive research has been conducted on a wide range of TMO anode materials encompassing unary (containing only one metal), binary and ternary oxides. [11-13] Materials containing Co, Mn, Ni, and Zn have been of particular interest and have been examined in various morphologies from nanoparticles to nanowires, core-shell structures and nanorods with promising results in terms of specific capacity values and cycle lifetimes. [14-17]

Nanostructuring of materials for Li-ion applications has allowed various performance issues associated with bulk materials to be mitigated. For example, the pulverisation of active materials caused by repeated expansion and contraction during cycling can be significantly improved by reducing materials below certain size thresholds. [18, 19] Similarly, introducing various levels of porosity into the material allows for enhanced electrolyte infiltration and reduced Li-ion diffusion distances, leading to improved high-rate performance. For this reason, inverse opals (IOs) have attracted significant interest as battery materials. [20-22] IOs are highly ordered structures with porosities defined by a pre-formed sphere template. These templates can be infilled with a wide range of precursors (usually a metal salt dissolved in a volatile solvent) with subsequent thermal treatment allowing the formation of various IO materials encompassing metals, TMOs and mixed TMOs. [23, 24] Given their large surface area, high degree of ordering and interconnected nature, IOs have been investigated for a wide range of applications, such as

catalysis and photonics. [25, 26] The versatility and promise of IO materials for battery applications was recently illustrated when we presented a full IO Li-ion cell comprised of pre-lithiated conversion mode Co_3O_4 anode and an intercalation mode V_2O_5 cathode. [27] This cell could be cycled for over 100 charge/discharge cycles with excellent capacity retention, and was a key illustration of IO structured active materials.

In this report, we investigate the fundamental electrochemical performance of Co_3O_4 IO anode materials in significantly more depth. This is achieved by comparing the performance of the IOs with microparticles (MPs) that are formed without the polystyrene sphere (PS) template necessary to form the IO structure. By contrasting the response of both material forms, we are able to show a clear improvement in performance by constraining the constituent nanoparticles into a three dimensional (3D) IO geometry. The rate-dependent characteristics of the IO anodes were examined through post-mortem scanning electron microscopy (SEM) analysis, revealing that high-rate galvanostatic charging of the conversion mode IO caused less structural changes compared to slower rate charging. Analysis of Raman spectroscopy and electron diffraction of a Co_3O_4 IO sample after 50 cycles indicated that Co_3O_4 is reduced and cycles reversibly as CoO. By comparing microparticles of Co_3O_4 to a Co_3O_4 nanoparticle network formed into a 3D open-worked inverse opal structure structures (both without additive or binders), we demonstrate that 3D IO Co_3O_4 can avoid unwanted cell inefficiencies and improve the consistency in charge-discharge rate, capacity retention, and cycle life.

2. Experimental Section

2.1 Materials synthesis

Co_3O_4 IO samples were prepared *via* infilling of a polystyrene (PS) sphere template. Initially a solution of PS spheres (Polysciences Inc., diameter = 500 nm) in isopropanol (IPA) was drop cast on to 1 cm^2 pieces of stainless steel; the sphere templates were then infilled with a 0.1 M solution of $CoCl_2$ in IPA. The infilled sphere templates where heated at 450 °C in air for 12 h, to remove the templates and to crystallize

the samples. Co_3O_4 MPs were prepared using the same method as the IOs except without the addition of the PS sphere template.

2.2 Materials characterization

Transmission electron microscopy (TEM) analysis was conducted using a JEOL JEM-2100 TEM operating at 200 kV. SEM analysis was performed using an FEI Quanta 650 FEG high resolution SEM at an accelerating voltage of 10 kV. Thermogravimetric analysis (TGA) was performed using a Mettler Toledo TGA/DSC1. Dried samples of the solution of $CoCl_2$ in IPA were placed in an alumina crucible and heated to 450 ºC in air at a heating rate of 5 ºC min^{-1}. X-ray diffraction (XRD) analysis was performed using a Phillips Xpert PW3719 diffractometer using Cu Kα radiation. (Cu Kα, λ = 0.15418 nm, operation voltage 40 kV, current 40 mA). X-ray photoelectron spectroscopy (XPS) spectra were acquired on an Oxford Applied Research Escabase XPS system equipped with a CLASS VM 100 mm mean radius hemispherical electron energy analyzer with multichannel detectors in an analysis chamber with a base pressure of 5.0×10^{-10} mbar. Survey scans were recorded between 0 and 1400 eV with a step size of 0.7 eV, dwell time of 0.5 s, and pass energy of 100 eV. Core level scans were acquired with a step size of 0.1 eV, dwell time of 0.5 s, and pass energy of 20 eV averaged over 10 scans. A non-monochromated Al Kα X-ray source at 200 W power was used for all scans. All spectra were acquired at a take-off angle of 90° with respect to the analyzer axis and were charge corrected with respect to the C 1s photoelectric line. Data was processed using CasaXPS software where a Shirley background correction was employed and peaks were fitted to Voigt profiles. Raman scattering was performed with a Renishaw InVia Raman Spectrometer using a 30 mW Ar^+ laser at 514 nm excitation. The beam was focused onto the samples using a 50× objective lens and spectra were collected using a RenCam CCD camera.

2.3. Electrochemical characterization

All electrochemical results presented in this report were performed using a BioLogic VSP Potentiostat/Galvanostat. The electrochemical properties of Co_3O_4 samples were investigated in a half cell

configuration against a pure Li counter electrode in a two electrode, stainless steel split cell (a coin cell assembly that can be disassembled for post-mortem analysis). The electrolyte used consisted of a 1 mol dm^{-3} solution of lithium hexafluorophosphate salt in a 1:1 (v/v) mixture of ethylene carbonate in dimethyl carbonate with 3 wt% vinylene carbonate. The separator used in all split cell tests was a glass fiber separator (El-Cell ECC1-01-0012-A/L, 18 mm diameter, 0.65 mm thickness). The mass loading for all Co_3O_4 samples was ~ 0.5 – 1.0 mg, no additional conductive additives or binders were added. Cyclic voltammetry was performed using a scan rate of 0.2 mV s^{-1} in a potential window of 3.0 – 0.01 V. Galvanostatic cycling was performed using a range of C rates (0.1 – 10 C) in a potential window of 3.0 – 0.01 V.

3. Results and Discussion

TEM and SEM images of Co_3O_4 MPs and IOs are shown in Figure 1. Co_3O_4 MPs are formed when the cobalt oxide precursor is dropcast on stainless steel substrates without a PS sphere template coating and then heated to 450 °C for 12 h. The diameter of the Co_3O_4 MPs is ~ 400 nm, as shown in Figure 1a. The MPs are an agglomeration of nanoparticles of Co_3O_4, with diameters of ~ 25 nm as shown in Figure 1b and c. Structurally, the Co_3O_4 MPs are quite similar to previously reported mesoporous Co_3O_4 cubes, which were prepared via a hydrothermal treatment of cobaltous acetate, carbamide and triethanolamine. [28] The Co_3O_4 IOs are formed when a PS sphere template is deposited on the stainless steel substrates prior to infilling with the cobalt oxide precursor solution. Thermal decomposition of the sacrificial PS sphere template resulted in a highly porous IO network with pore sizes of ~ 400 nm. The walls of the IO structure are comprised of an assembly of nanoparticles, as shown in Figure 1f. Interestingly the nanoparticles that comprise the walls of the IO have smaller diameters (~ 10 nm) than the nanoparticles that make up the disordered MPs. It is possible that confining the cobalt oxide precursor solution between the PS sphere template may limit the growth of the Co_3O_4 nanoparticles during calcination, resulting in a smaller particle size, and this is characteristic of several metal oxides we grow as IO structures from solution-based precursors. Additional SEM images of the Co_3O_4 IOs are shown in Figure S1. The electron

diffraction patterns for both Co_3O_4 MPs and IO consisted of a series of diffraction rings, indicating their polycrystalline structure, as shown in Figure 1d and h respectively. Both patterns were successfully indexed to pure fcc Co_3O_4, confirming that the MPs and IO represent disordered and highly ordered variants of the same material.

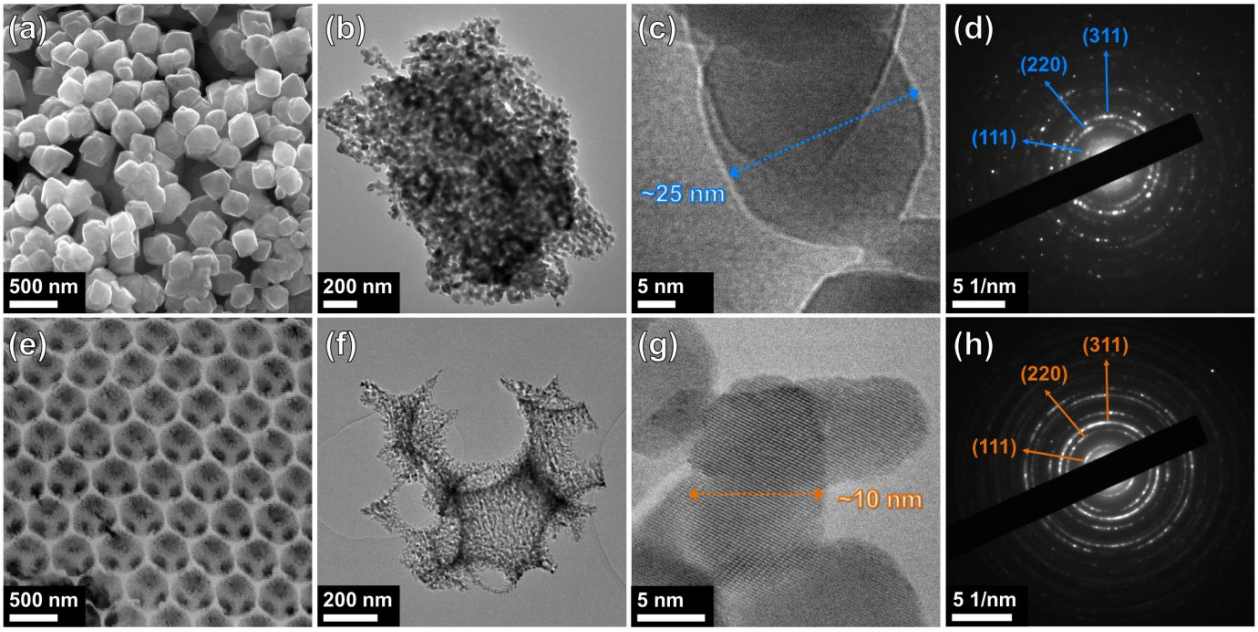


Figure 1. (a) SEM image, (b) and (c) TEM images and (d) electron diffraction pattern for Co_3O_4 MPs. (e) SEM image, (f) and (g) TEM images and (h) electron diffraction pattern for Co_3O_4 IO.

Thermogravimetric analysis of the cobalt oxide precursor used to prepare the Co_3O_4 MPs and the IO indicates that ~ 43% mass is lost when heated to 475 °C in air, as shown in Figure 2a. The mass loss occurs in 4 discrete steps. Initially, ~ 20% mass is lost during heating from 25 – 63 °C, 2% mass is lost from 63 – 100 °C, 12% lost from 100 – 120 °C and 8% mass is lost from 120 – 160 °C. Only ~ 1% mass is subsequently lost during heating from 160 – 450 °C, during crystallization stage. The observed mass losses are in close agreement with previous studies on the thermal dehydration and decomposition of cobalt chloride, [29] which was used as the precursor for both Co_3O_4 MPs and IO samples. The initial mass losses up to ~ 63 °C are most likely due to the removal of physisorbed water. Mass losses from 63 – 160 °C may be attributed to the removal of chemisorbed water and the thermal decomposition of $CoCl_2$.

The XRD patterns for the Co_3O_4 MPs and the IO are shown in Figure 2b. The reflections observed in both XRD patterns can be readily indexed to pure fcc Co_3O_4 (JCPDS No. 42-1467) with a *Fd3m* space group, confirming that the MPs and the IO are both Co_3O_4 with identical crystalline phase as nanoscale crystallites, and thus the synthesises successfully formed both a disordered MP agglomerate and a 3D structured IO variant. The reduced intensity and broader diffraction peaks from the IO confirm TEM data of a smaller nanocrystal size that make up the walls of the IO structure. The crystallinity is maintained when a 3D IO structure is imposed on the decomposition and crystallization of the precursor to Co_3O_4, with no detectable influence of the calcined polymer spheres on the phase or composition.

XPS spectra for a Co_3O_4 IO sample are presented in Figure 2c and d. The Co $2p_{3/2}$ and $2p_{1/2}$ levels were observed in the Co 2p spectrum at ~ 780.2 and 795.4 eV, respectively, which is in excellent agreement with previous reports for other Co_3O_4 nanostructures. [30, 31] Satellite peaks for the $2p_{3/2}$ and $2p_{1/2}$ levels were observed at ~ 788.8 and 804.5 eV, which again is in close agreement with previous studies. [32-34] It is likely that both Co^{2+} and Co^{3+} are present in the Co_3O_4 IO structure, as indicated by the deconvoluted peaks for the Co $2p_{3/2}$ and $2p_{1/2}$ levels and the satellite peaks shown in Figure 2c. Analysis of the deconvoluted peaks indicates that ~ 76% of the cobalt present was in the Co^{3+} valence state. Three oxygen contributions were observed in the high resolution spectrum for the O 1s shows, shown in Figure 2d. The peak at ~ 529.8 eV is typical of metal-oxygen bonds [35, 36], while the peak at ~ 531.4 eV can be attributed to oxygen vacancy defects and a number of surface species including chemisorbed oxygen or under-coordinated lattice oxygen and hydroxyls. [37, 38] The peak observed at ~ 533.2 eV can be ascribed to a multiplicity of physi- and chemisorbed water at or near the surface. [35, 36] As electron diffraction for individual NPs and XRD for the bulk quantities of both MPs and IOs indicate the spinel Co_3O_4 phase, the XPS confirms that surface defects and species common to transition metal oxides do exist on both structure.

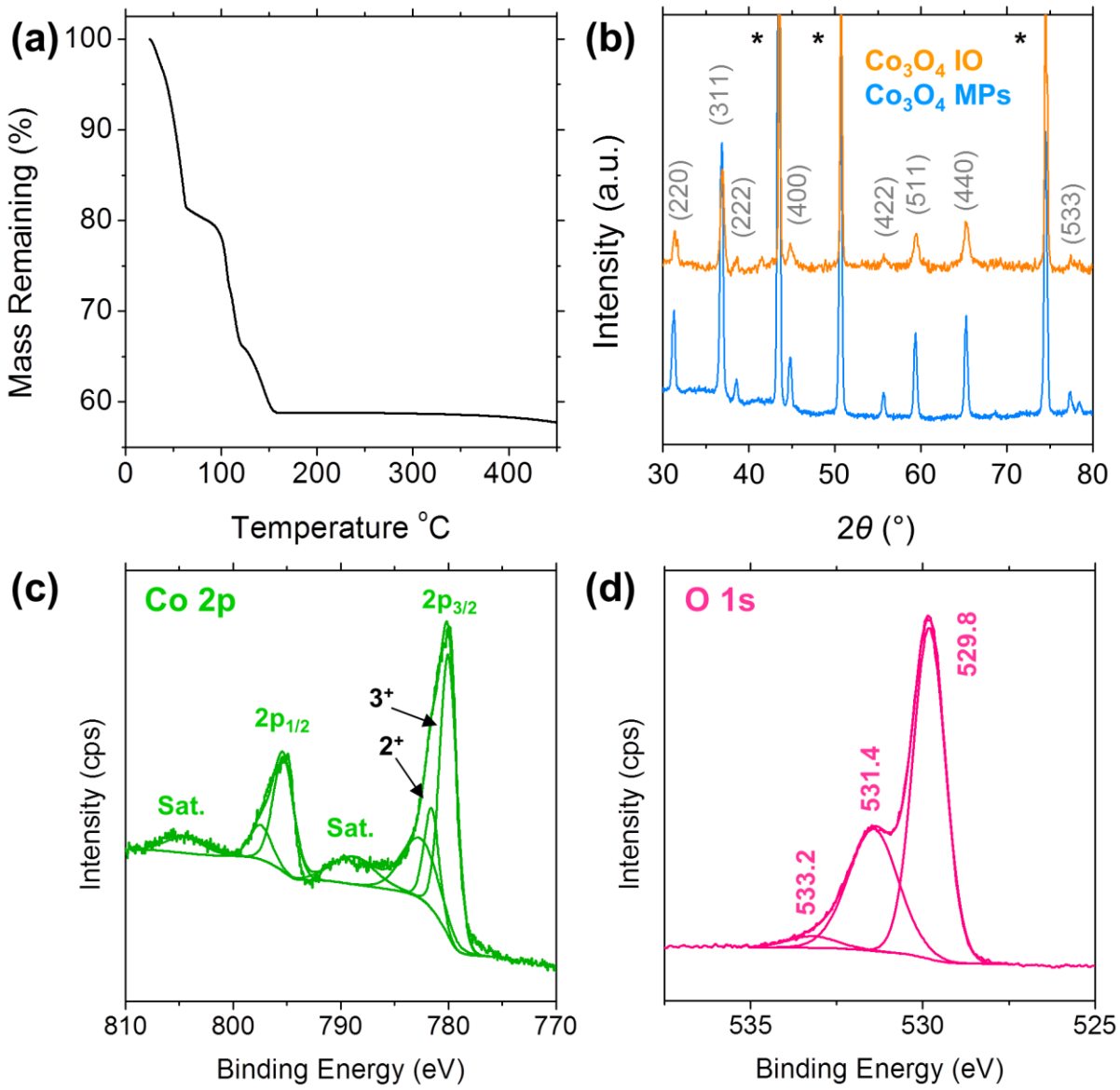


Figure 2. (a) Thermogravimetric analysis mass loss curves for cobalt oxide precursor heated to 450 °C in air at a ramp rate of 5 °C/min. (b) XRD patterns for Co_3O_4 MPs and IOs prepared on stainless steel substrates (reflections labelled * are stainless steel peaks). XPS spectra of the (c) Co 2p and (d) O 1s core-level photoemission from Co_3O_4 IO.

The nature of the phase and composition of Co_3O_4 conversion mode anodes, their modification during charging and discharging and relationship to cell voltage, capacity, side reactions and stability are important considerations to the cell response of materials that reply on displacement reactions. A comparison of cyclic voltammograms acquired for Co_3O_4 MP and IO samples are shown in Figure 3. A

sharp reduction peak was observed in the first cathodic scan for Co_3O_4 MPs ~ 0.62 V, as shown in Figure 3a. The initial reduction peak for Co_3O_4 IO, however, is found at a slightly more positive potential of ~ 0.88 V, followed by a weak shoulder peak at ~ 0.74 V, as shown in Figure 3b, due to the smaller nanocrystal size [39] (Figure 1c and g). The strong cathodic peak for both the Co_3O_4 MPs and IO samples corresponds to the reduction of Co_3O_4 and the formation of amorphous Li_2O and the SEI layer [40]. It has previously been reported that during the first charge Co_3O_4 undergoes an irreversible reduction [28, 41-43] as given by:

$$Co_3O_4 + 8Li^+ + 8e^- \rightarrow 3Co + 4Li_2O \qquad (1)$$

Consequently, this suggests that Co_3O_4 MPs and IO are decomposed into a composite consisting of nanosized grains of Co embedded in a Li_2O matrix. In the second voltammetric scan, the reduction peak shifted by 18 mV to a higher potential of ~ 0.80 V for the Co_3O_4 MPs, but the Co_3O_4 IO peak shift was just 8 mV to ~ 0.96 V, ensuring that IO NP structures are more easily reduced. Co_3O_4 is known to behave as a conversion mode material, i.e. Co_3O_4 is reduced to form Co metal and during the subsequent anodic scan Co is reoxidised. It has previously been reported that the nanoparticles of CoO that are formed during the anodic scan can be quite small (~5 nm) and are not reoxidized fully back to spinel Co_3O_4. [44, 45] The small shift in reduction peak to higher potentials from the second scan may also be due to the reduced particle size of the CoO phase once formed after the first anodic scan. [46]

Two anodic peaks were observed at in first scan for Co_3O_4 MPs and IO samples at ~ 1.65 and 2.05 V, which may be attributed to the oxidation of Co to CoO and the decomposition of Li_2O as follows:

$$Co + Li_2O \rightarrow CoO + 2Li^+ + 2e^- \qquad (2)$$

Following the initial reduction of Co_3O_4 and formation of a stable CoO phase the Li reaction mechanism can be described as follows:

$$CoO + 2Li^+ + 2e^- \leftrightarrow Co + Li_2O \qquad (3)$$

Previous studies have suggested that the initial reduction of Co_3O_4 to form Co^0 may not be an irreversible reaction [47], i.e. during the anodic scan as described by equation (2), some of the CoO formed may be further oxidized to Co_3O_4. We will investigate this further in the analysis of the Raman spectra after the first charge and discharge.

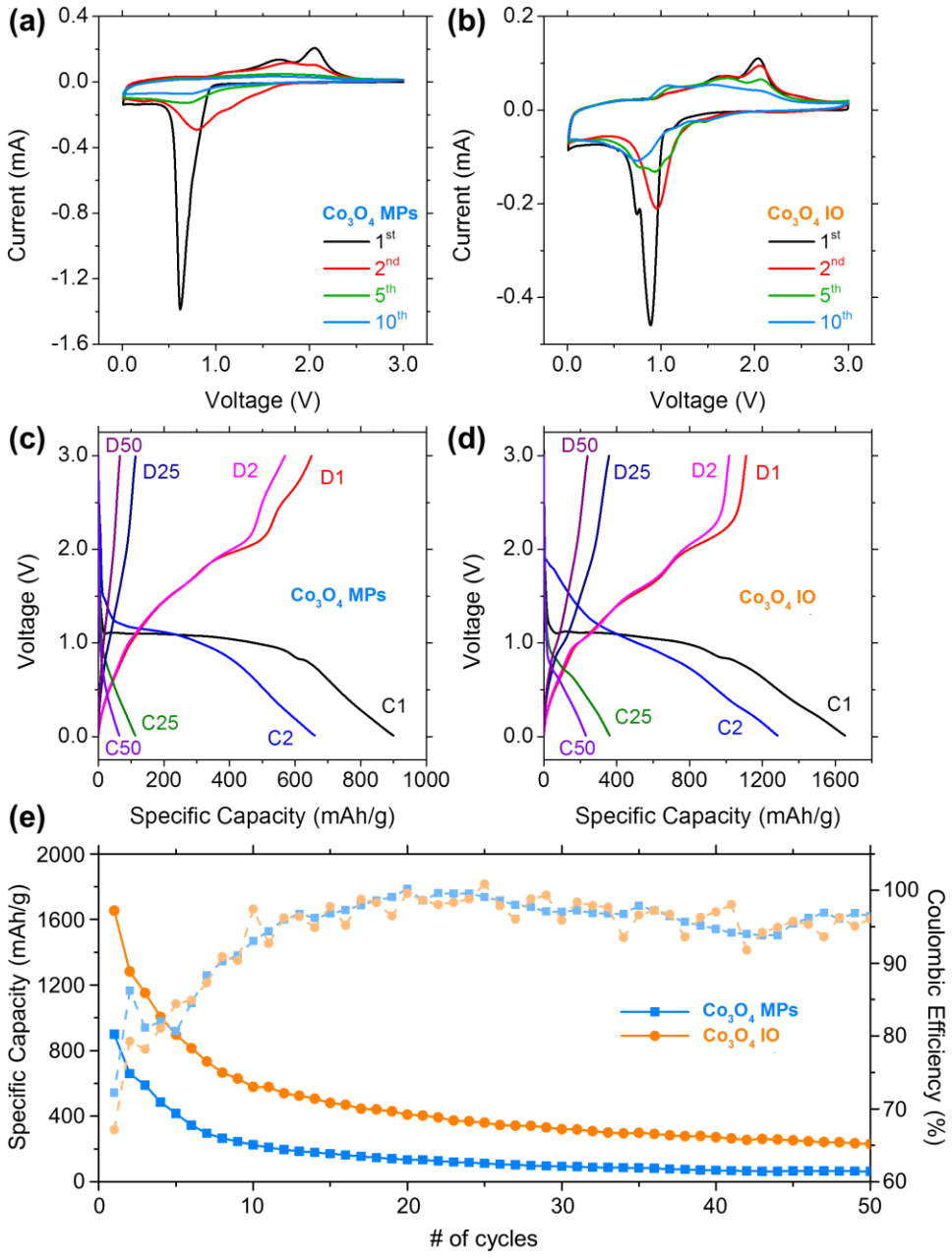


Figure 3. Cyclic voltammograms for (a) Co_3O_4 MPs and (b) Co_3O_4 IO, acquired at a scan rate of 0.2 mV s^{-1}. Charge and discharge voltage profiles for the 1st, 2nd, 25th and 50th cycles for (c) Co_3O_4 MPs and (d) Co_3O_4 IO at a C rate of 0.1 C in a potential window of 3.0 – 0.01 V. (e) Comparison of the specific capacity values and Coulombic efficiency obtained for Co_3O_4 MPs and IO over 50 cycles.

Galvanostatic tests were performed to determine the effects of particle size and ordering of Co_3O_4 samples on specific capacity values and capacity retention. The galvanostatic charge and discharge curves for the 1st, 2nd, 25th and 50th cycles for Co_3O_4 MPs and IO samples at a C/10 rate are shown in Figure 3c and d, respectively. A characteristic long voltage plateau was observed in the initial charge curve for both samples between 1.1 and 0.8 V, corresponding to the reduction of Co_3O_4 to CoO and Co^0, (equation (1)) which is in close agreement with the potential at which the strong reduction peak occurred in the first cathodic CV scan for each sample, shown in Figure 3a and b. Following from the long plateau a sloping region from 0.8 to the lower voltage limit of 0.01 V was observed for both samples. The sloping region may be attributed to the formation of amorphous Li_2O and an SEI layer. The plateau observed in the first discharge curve for both the Co_3O_4 MPs and IO samples from ~ 1.6 – 2.1 V, corresponds to the oxidation of Co^0 to CoO as explained by equation (2). The voltage profile of the 2nd charge does not contain the long plateau which was observed during the first charge, and a sloping curve was observed instead. The profile of this first charge curve is quite similar to previously reported charge profiles for CoO anode materials [48, 49], which indicates that the Co_3O_4 IO actually avoids reduction to metallic Co^0 entirely, allowing the anode material to charge and discharge via the reversible reduction and oxidation of CoO, which reduces the overpotential for reversible Li_2O formation and decomposition during cycling.

A comparison of the specific capacity values obtained over 50 cycles for Co_3O_4 MPs and IO samples is shown in Figure 3e. It is immediately clear that the highly ordered IO structure offered significantly higher specific capacity values compared to the disordered collection of MPs. The initial capacity for the Co_3O_4 IO was ~ 1655 mAh/g, which is significantly higher than the theoretical capacity of 890 mAh/g. It has previously been reported that heating transition metal oxides in air can introduce defects, such as cation vacancies associated with lithiated oxygen sites, which can electrochemically exchange Li ions and serve as additional charge-storage sites. [50] The presence of any such defects after heating the Co_3O_4 samples to 450 °C may result in an initial increased capacity. With electrolyte decomposition effect, consequently, the irreversible capacity loss is characteristically significant after the

first charge. In addition to this the high initial specific capacity may also be attributed to the formation of an SEI layer. [51] The specific capacity for the second charge decreased to ~ 1285 mAh/g. The capacity values for the Co_3O_4 IO sample after the 25^{th} and 50^{th} cycles were ~ 360 and 230 mAh/g respectively, attaining a stable value.

The initial specific capacity of the Co_3O_4 MPs (~ 900 mAh/g) was much lower than for the IO. Analysis of electron diffraction and XRD patterns for the MPs and IOs confirms that both samples are pure Co_3O_4. Hence Figure 3e indicates that the ordering and particle size of Co_3O_4 samples has a significant effect on their electrochemical performance. The specific capacity is enhanced by the open-worked macroporous structuring of Co_3O_4 IO, compared to the agglomerated MP structure. The disordered Co_3O_4 MPs suffer severe capacity fading with capacity values of ~ 660, 110 and 65 mAh/g after the 2^{nd}, 25^{th} and 50^{th} cycles respectively. Capacity fading issues have been previously reported for conversion mode materials, hence many researchers prepare composites of conversion mode materials with graphene. [5] The initial irreversible capacity loss is due to the significant change in the phase of the Co_3O_4, from a complex compound to an unary metal. An article by Wu et al. compared the performance of Co_3O_4 nanoparticles on their own and in a composite with graphene. [17] They reported that when cycled on their own the Co_3O_4 nanoparticles suffered from severe capacity fading and their performance was significantly enhanced by preparing a composite with graphene. However, they also demonstrated that high capacity values can be obtained from the graphene sheets cycled on their own. Graphene stores charge and significantly contributes to the capacity values obtained.

We desired to investigate the fundamental electrochemical response of our Co_3O_4 samples in the absence of any materials which actively contribute towards the total charge stored. The capacity retention of our Co_3O_4 samples was improved by engineering nanoparticles into an IO architecture. Even though Co_3O_4 is a conversion mode material, cycling of electrolyte-accessible CoO phase with the parallel formation and dissolution of Li_2O that must be stored and removed (IOs have reduced mass transport

limitations and clogging by Li_2O compared to the 3D IO), the initial ordering of the sample has a profound influence on its electrochemical behaviour.

It has previously been reported that the capacity values of nanostructured Co_3O_4 samples can be significantly enhanced by preparing composites with graphene and various other forms of carbon. [17, 52] It is well known that carbon is electrochemically active toward intercalation within the potential window that Co_3O_4 is cycled in [53], and so may also be contributing to the increased capacity. We desired to determine the fundamental effects of particle size, morphology and ordering on the electrochemical performance of our Co_3O_4 samples and consequently tests were performed in the absence of any conductive additives which may be contributing towards the charge stored. Further to this, preparing composites with graphene or slurries with other conductive additives would block the pores of the IO structure making it difficult to assess the contribution of the porous interconnected structure towards the performance of the material.

In order to investigate the reduction process and the subsequent oxidation and cycling, Raman spectra of an as prepared Co_3O_4 IO and an IO after the first charge and discharge (at 0.1 C) were acquired, as shown in Figure 4. The Raman spectrum for the as prepared Co_3O_4 IO contains five distinct peaks at ~ 196, 484, 524, 620 and 692 cm^{-1}, corresponding to the F^1_{2g}, E_g, F^2_{2g}, F^3_{2g} and A_{1g} modes of crystalline Co_3O_4, respectively. [54] After the first charge the five peaks were shifted to lower wavenumbers of ~ 191, 472, 518, 608 and 675 cm^{-1}, respectively. The Raman shift values after the first charge are in close agreement with previously reported Raman spectra for CoO, [55] indicating that the initial Co_3O_4 is only partially reduced to CoO after the first charge; i.e. not fully reduced to Co^0. Consequently, it may take a number of cycles before all of the Co_3O_4 present is fully reduced and CoO is cycled reversibly, as observed in Figure 3e also. We propose an addition to equation (1) whereby Co_3O_4 is partially reduced to both CoO and Co^0 as follows:

$$Co_3O_4 + 4Li^+ + 4e^- \rightarrow 2CoO + Co + 2Li_2O \qquad (4)$$

It has previously been reported that there is a Raman band for Li_2O at ~ 522 cm^{-1}. [56] After the first charge the relative intensity of the F^2_{2g} mode is higher than that of the E_g mode, the opposite was the case for the as-prepared Co_3O_4 IO. When the proximity of the broad F^2_{2g} mode (from ~ 500 to 535 cm^{-1}) is taken into account, it is possible that the Raman band for Li_2O may be convoluted into the band corresponding to the F^2_{2g} mode. After the first discharge, two strong peaks were observed at ~ 519 and 691 cm^{-1}. The first peak is a close match to the F^2_{2g} mode of crystalline Co_3O_4. The second, wide band can be deconvoluted into two distinct peaks centred at 667.9 and 694.4 cm^{-1}, as shown in Figure S2. This suggests that the wide band is a convolution of the strong bands observed in the Raman spectra for the as prepared Co_3O_4 IO and the IO after the first charge. This indicates that after the first discharge both Co_3O_4 and CoO may be present. The broadening and shifting of the Co_3O_4 Raman bands after the first discharge may also be indicative of a decreased particle size. Choi et al. previously reported on size effects in the Raman spectra of TiO_2 nanoparticles, whereby decreasing particle size resulted in a broadening of Raman bands which were also shifted to lower wavenumbers. [57] The presence of F^2_{2g} and A_{1g} modes of Co_3O_4 after the first discharge, indicates that CoO is oxidised back to Co_3O_4. This again supports our suggestion that it may take several cycles before all of the Co_3O_4 is fully reduced to Co^0 and the redox process as described by equation (3) dominates the electrochemical reaction. To investigate this further a Raman spectrum was acquired for a Co_3O_4 IO sample after 50 cycles. The three peaks at 478, 609 and 690 cm^{-1} can be attributed to the presence of CoO and are in close agreement with the peaks observed after the 1st charge. Co^0 formed during the 50th charge was likely oxidised to CoO during the 50th discharge, resulting in the presence of CoO observed in the Raman spectrum after 50 cycles. Additionally the peak at ~ 521 cm^{-1} is due to the presence of Li_2O. Observing Li_2O after the 50th discharge may indicate that there are regions of Li_2O which were not reduced during the 50th charge. With increased cycling some regions of the electrode may become electrically inactive, which may also contribute towards the capacity fading issues observed in Figure 3e.

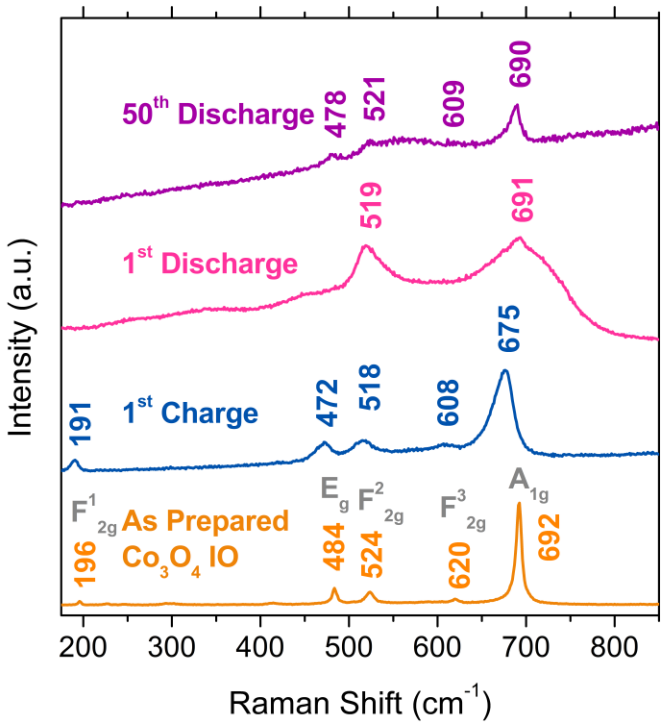


Figure 4. Raman spectra for an as prepared Co_3O_4 IO and a Co_3O_4 IO after the 1st charge, the 1st discharge and the 50th discharge at a C rate of 0.1 C in a potential window of 3.0 – 0.01 V.

In order to determine what effect the initial reduction of Co_3O_4 would have on the morphology of the Co_3O_4 IO, four different IO samples were charged at C rates of 0.1 C, 1 C, 5 C and 10 C, as shown in Figure 5. A comparison of the resulting specific capacity values is shown in Figure 5a. The initial specific capacity increased with decreasing C rate with values of ~ 525, 755, 1535 and 1684 mAh/g for C rates of 10 C, 5 C, 1 C and 0.1 C, respectively. The IO structure on the surface of the sample was no longer present after the first charge at the slowest C rate used (0.1 C), instead nanoparticles of CoO and Co^0 were present. The matrix of Co^0 nanoparticles is still quite porous as can be seen in Figure 5b, hence the advantage that the IO structure offers over other nanostructures in terms of porosity is still preserved to some degree. After the first charge at 1 C, the IO structure shown in Figure 1e is also no longer present. This sample has regions containing similar nanoparticles to those observed in Figure 5b as well as areas with thick, collapsed IO walls, as shown in Figure 5c. Similar to the IO charged at a 0.1 C rate, there is still some evidence of porosity. The highly ordered, 3D IO structure is no longer evident. After the first

charge at 5 C, the walls of the IO have significantly swollen due to Li_2O formation. Volumetric contraction occurs during the Co_3O_4 reduction and oxidation as it molar volume is ~2× that of Co. However, the pores of the IO are noticeably maintained, as shown in Figure 5d. The IO structure was best preserved after the first charge at 10 C. The walls of the IO are not as swollen as the after the first charge at 5 C and the pores are also much wider, as can be seen in Figure 5e.

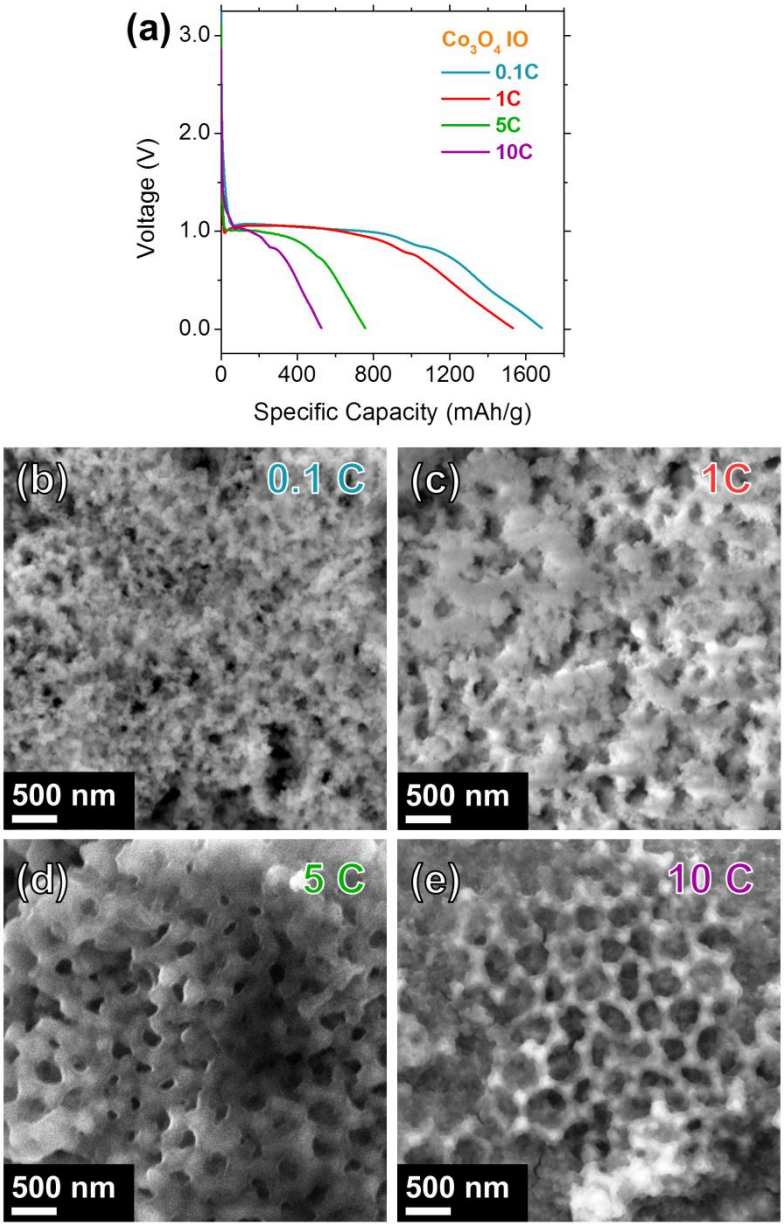


Figure 5. (a) Comparison of the voltage profiles for the 1st charge for Co_3O_4 IO samples cycled at 0.1C, 1 C, 5 C and 10 C. SEM images of Co_3O_4 IO samples after the 1st charge at a C rate of (b) 0.1 C, (c) 1 C, (d) 5 C and (e) 10 C.

From Figure 5 it is clear that faster C rates are less destructive to the IO structure after the first charge. The SEM images presented are of the surface of the IO samples, it is possible that other regions further into the initial islands of IO, as shown in Figure S1, may retain the IO structure after the first charge. Further to this, the retention of the IO structure at the fastest C rate used (10 C) may explain the lower initial specific capacity values obtained, i.e. the IO morphology may be maintained due to only a partial reduction of Co_3O_4 to CoO. Interestingly, even though the IO structure is maintained after the first charge at 10 C, the highest capacity values were obtained at 0.1 C when the IO structure was destroyed and converted to a matrix of CoO nanoparticles in Li_2O after the first charge. We surmise that the rate of Li_2O formation limits the capacity and as the capacity is related to the volume of Li_2O, also minimizes the changes to the IO structure and avoids clogging electrode and thus ensuring Li_2O decomposition.

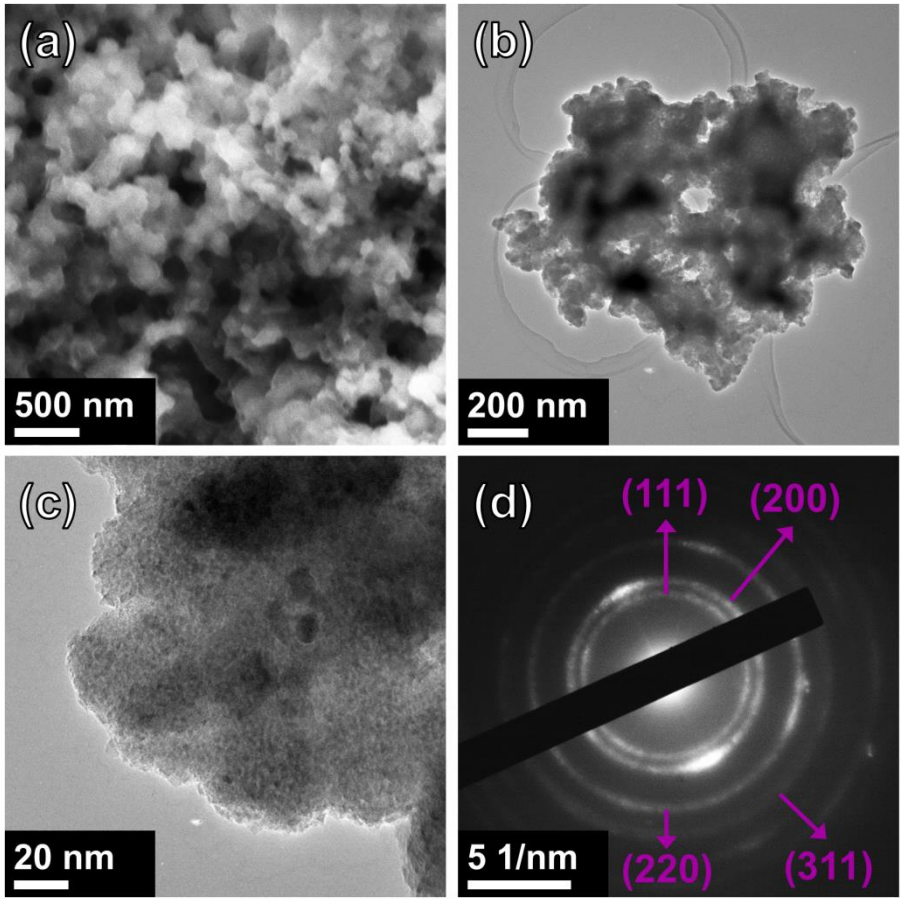


Figure 6. (a) SEM and (b) and (c) TEM images of a Co_3O_4 IO sample after 50 cycles. (d) Electron diffraction pattern of a Co_3O_4 IO sample after 500 cycles

SEM and TEM images of a Co_3O_4 IO sample after 50 cycles are shown in Figure 6a,b and c respectively. Similar to the Co_3O_4 IO samples after the first charge at slower C rates (0.1 and 1 C), after 500 cycles the IO structure has been converted into an agglomeration of nanoparticles. Raman analysis of the Co_3O_4 IO sample after 500 cycles, presented in Figure 4, suggests that the nanoparticles are CoO. In order to further investigate this, an electron diffraction pattern for a Co_3O_4 IO sample after 50 cycles was acquired as shown in Figure 6d. The electron diffraction pattern consisted of a series of diffraction rings, indicating after 50 cycles the sample has a polycrystalline structure and has not become amorphous. The electron diffraction pattern was successfully indexed to pure cubic CoO (JCPDS No. 00-048-1719) with a *Fm-3m* space group. The presence of CoO after the 50^{th} discharge is in close agreement with equation (3) and confirms that with increased cycling Co_3O_4 is reduced and CoO is reversibly cycled.

4. Conclusions

Conversion mode Co_3O_4 anode performance can be significantly improved by structuring nanocrystalline material in an open 3D inverse opals structure. Li_2O formation and decomposition is kinetically limited at faster C-rates, and is efficiently and reversibly formed within an IO structure, improving capacity retention and overpotential. From galvanostatic testing it is clear that the ordered IO structure offered significantly higher specific capacity values compared to the disordered collection of Co_3O_4 MPs. We demonstrated that the electrochemical performance of our Co_3O_4 samples can be greatly improved by organizing assemblies of Co_3O_4 nanoparticles into an inverse opal architecture. Conversion mode reactions can be quite destructive to the initial structure, due to a reduction to an unary metal. Our results indicate that despite the destructive nature of this conversion reaction mechanism, the initial ordering of the Co_3O_4 samples has a profound influence on its electrochemical behaviour, capacity retention, energy efficiency and rate performance. Raman scattering analysis of a pristine Co_3O_4 IO and an IO after the first charge and discharge indicates that the initial Co_3O_4 may only be partially reduced to CoO after the first charge. SEM analysis of Co_3O_4 IO samples after the first charge indicates that faster C rates are less

destructive to the IO structure charge. Interestingly however the highest capacity values were obtained at the slowest rate investigated (0.1 C) when the IO structure was destroyed and converted to a matrix of CoO nanoparticles and Li_2O after the first charge.

This result offers useful insight into the morphology of nanostructured conversion mode anode materials, whereby the sample which underwent the most severe alteration of the initial IO structure ultimately provided the highest specific capacity values, even with some fading during cycling because of the mass transport improvement form the open-worked IO structure. The same may not be true for anode materials with other Li reaction mechanisms, such as intercalation and alloying materials where it may be beneficial to maintain the initial structure. Cycling at 0.1 C results in a capacity of ~ 250 mAh/g after 50 cycles, making Co_3O_4 IOs an efficient conversion mode anode. Raman spectroscopy, electron microscopy and electron diffraction confirm that after 50 cycles the Co_3O_4 IO is reduced to an agglomeration of CoO nanoparticles. The Li_2O phase formed within the IO structure at faster rates is highly reversible, with clogging of the pores and capacity fading being significantly reduced to a relatively stable and useful value.

Acknowledgements

This work was also supported by Science Foundation Ireland (SFI) through an SFI Technology Innovation and Development Award under contract no. 13/TIDA/E2761. This publication has also emanated from research supported in part by a research grant from SFI under Grant Number 14/IA/2581.

References

[1] Agostini M, Brutti S and Hassoun J 2016 High Voltage Li-Ion Battery Using Exfoliated Graphite/Graphene Nanosheets Anode *ACS Appl. Mater. Interfaces* **8** 10850–7

[2] Chen J, Zou G, Zhang Y, Song W, Hou H, Huang Z, Liao H, Li S and Ji X 2016 Activated Flake Graphite Coated with Pyrolysis Carbon as Promising Anode for Lithium Storage *Electrochim. Acta* **196** 405-12

[3] Deng T and Zhou X 2016 The Preparation of Porous Graphite and its Application in Lithium Ion Batteries as Anode Material *J. Solid State Electrochem.* **20** 2613–8

[4] Yoshio M, Wang H, Fukuda K, Hara Y and Adachi Y 2000 Effect of Carbon Coating on Electrochemical Performance of Treated Natural Graphite as Lithium-Ion Battery Anode Material *J. Electrochem. Soc.* **147** 1245-50

[5] Cabana J, Monconduit L, Larcher D and Palacín M R 2010 Beyond Intercalation-Based Li-Ion Batteries: The State of the Art and Challenges of Electrode Materials Reacting Through Conversion Reactions *Adv. Mater.* **22** E170-E92
[6] Chae B-M, Oh E-S and Lee Y-K 2015 Conversion Mechanisms of Cobalt Oxide Anode for Li-ion Battery: In situ X-ray Absorption Fine Structure Studies *J. Power Sources* **274** 748-54
[7] Liu J, Kelly S J, Epstein E S, Pan Z, Huang X, Liu J and Braun P V 2015 Three-dimensionally Scaffolded Co_3O_4 Nanosheet Anodes with High Rate Performance *J. Power Sources* **299** 40-8
[8] Fu C, Li G, Luo D, Huang X, Zheng J and Li L 2014 One-Step Calcination-Free Synthesis of Multicomponent Spinel Assembled Microspheres for High-Performance Anodes of Li-Ion Batteries: A Case Study of $MnCo_2O_4$ *ACS Appl. Mater. Interfaces* **6** 2439-49
[9] Malini R, Uma U, Sheela T, Ganesan M and Renganathan N G 2008 Conversion Reactions: A New Pathway to Realise Energy in Lithium-ion Battery - Review *Ionics* **15** 301-7
[10] Wang C, Yin L, Xiang D and Qi Y 2012 Uniform Carbon Layer Coated Mn_3O_4 Nanorod Anodes with Improved Reversible Capacity and Cyclic Stability for Lithium Ion Batteries *ACS Appl. Mater. Interfaces* **4** 1636-42
[11] Ji L, Lin Z, Alcoutlabi M and Zhang X 2011 Recent Developments in Nanostructured Anode Materials for Rechargeable Lithium-ion Batteries *Energy Environ. Sci.* **4** 2682-99
[12] Reddy M V, Subba Rao G V and Chowdari B V R 2013 Metal Oxides and Oxysalts as Anode Materials for Li Ion Batteries *Chem. Rev.* **113** 5364-457
[13] Wu H B, Chen J S, Hng H H and Wen Lou X 2012 Nanostructured Metal Oxide-Based Materials as Advanced Anodes for Lithium-ion Batteries *Nanoscale* **4** 2526-42
[14] Cai D, Wang D, Liu B, Wang L, Liu Y, Li H, Wang Y, Li Q and Wang T 2014 Three-Dimensional Co_3O_4@$NiMoO_4$ Core/Shell Nanowire Arrays on Ni Foam for Electrochemical Energy Storage *ACS Appl. Mater. Interfaces* **6** 5050-5
[15] Huang G, Xu S, Xu Z, Sun H and Li L 2014 Core–Shell Ellipsoidal $MnCo_2O_4$ Anode with Micro-/Nano-Structure and Concentration Gradient for Lithium-Ion Batteries *ACS Appl. Mater. Interfaces* **6** 21325-34
[16] Wu M-S and Chang H-W 2013 Self-Assembly of NiO-Coated ZnO Nanorod Electrodes with Core–Shell Nanostructures as Anode Materials for Rechargeable Lithium-Ion Batteries *J. Phys. Chem. C* **117** 2590-9
[17] Wu Z-S, Ren W, Wen L, Gao L, Zhao J, Chen Z, Zhou G, Li F and Cheng H-M 2010 Graphene Anchored with Co_3O_4 Nanoparticles as Anode of Lithium Ion Batteries with Enhanced Reversible Capacity and Cyclic Performance *ACS Nano* **4** 3187-94
[18] Li X, Gu M, Hu S, Kennard R, Yan P, Chen X, Wang C, Sailor M J, Zhang J-G and Liu J 2014 Mesoporous Silicon Sponge as an Anti-Pulverization Structure for High-Performance Lithium-ion Battery Anodes *Nat. Commun.* **5** 4105
[19] Tao H-C, Fan L-Z and Qu X 2012 Facile Synthesis of Ordered Porous Si@C Nanorods as Anode Materials for Li-ion Batteries *Electrochim. Acta* **71** 194-200
[20] Armstrong E and O'Dwyer C 2015 Artificial Opal Photonic Crystals and Inverse Opal Structures - Fundamentals and Applications from Optics to Energy Storage *J. Mater. Chem. C* **3** 6109-43
[21] O'Dwyer C 2016 Color-Coded Batteries – Electro-Photonic Inverse Opal Materials for Enhanced Electrochemical Energy Storage and Optically Encoded Diagnostics *Adv. Mater.* **28** 5681–8
[22] Osiak M, Geaney H, Armstrong E and O'Dwyer C 2014 Structuring Materials for Lithium-ion Batteries: Advancements in Nanomaterial Structure, Composition, and Defined Assembly on Cell Performance *J. Mater. Chem. A* **2** 9433-60
[23] Armstrong E, McNulty D, Geaney H and O'Dwyer C 2015 Electrodeposited Structurally Stable V_2O_5 Inverse Opal Networks as High Performance Thin Film Lithium Batteries *ACS Appl. Mater. Interfaces* **7** 27006-15
[24] Vu A, Qian Y and Stein A 2012 Porous Electrode Materials for Lithium-Ion Batteries – How to Prepare Them and What Makes Them Special *Adv. Energy Mater.* **2** 1056-85

[25] Aguirre C I, Reguera E and Stein A 2010 Tunable Colors in Opals and Inverse Opal Photonic Crystals *Adv. Func. Mater.* **20** 2565-78
[26] Dusastre V 2013 Inverse Opal Catalysts *Nat. Mater.* **12** 1080-
[27] McNulty D, Geaney H, Armstrong E and O'Dwyer C 2016 High Performance Inverse Opal Li-ion Battery with Paired Intercalation and Conversion Mode Electrodes *J. Mater. Chem. A* **4** 4448-56
[28] Huang G, Xu S, Lu S, Li L and Sun H 2014 Micro-/Nanostructured Co_3O_4 Anode with Enhanced Rate Capability for Lithium-Ion Batteries *ACS Appl. Mater. Interfaces* **6** 7236-43
[29] Mishra S K and Kanungo S B 1992 Thermal Dehydration and Decomposition of Cobalt Chloride Hydrate ($CoCl_2 \cdot xH_2O$) *J. Therm. Anal.* **38** 2437-54
[30] Chuang T J, Brundle C R and Rice D W 1976 Interpretation of the X-ray Photoemission Spectra of Cobalt Oxides and Cobalt Oxide Surfaces *Surf. Sci.* **59** 413-29
[31] Yan C, Chen G, Zhou X, Sun J and Lv C 2016 Template-Based Engineering of Carbon-Doped Co_3O_4 Hollow Nanofibers as Anode Materials for Lithium-Ion Batteries *Adv. Func. Mater.* **26** 1428-36
[32] Dong Z, Fu Y, Han Q, Xu Y and Zhang H 2007 Synthesis and Physical Properties of Co_3O_4 Nanowires *J. Phys. Chem. C* **111** 18475-8
[33] Hou L, Yuan C, Yang L, Shen L, Zhang F and Zhang X 2011 Urchin-like Co_3O_4 Microspherical Hierarchical Superstructures Constructed by One-Dimension Nanowires Toward Electrochemical Capacitors *RSC Adv.* **1** 1521-6
[34] Varghese B, Teo C H, Zhu Y, Reddy M V, Chowdari B V R, Wee A T S, Tan V B C, Lim C T and Sow C H 2007 Co_3O_4 Nanostructures with Different Morphologies and their Field-Emission Properties *Adv. Func. Mater.* **17** 1932-9
[35] Choudhury T, Saied S O, Sullivan J L and Abbot A M 1989 Reduction of Oxides of Iron, Cobalt, Titanium and Niobium by Low-Energy Ion Bombardment *J. Phys. D* **22** 1185-95
[36] Marco J F, Gancedo J R, Gracia M, Gautier J L, Ríos E and Berry F J 2000 Characterization of the Nickel Cobaltite, $NiCo_2O_4$, Prepared by Several Methods: An XRD, XANES, EXAFS, and XPS Study *J. Solid State Chem.* **153** 74-81
[37] Roginskaya Y E, Morozova O V, Lubnin E N, Ulitina Y E, Lopukhova G V and Trasatti S 1997 Characterization of Bulk and Surface Composition of $Co_xNi_{1-x}O_y$ Mixed Oxides for Electrocatalysis *Langmuir* **13** 4621-7
[38] Zhong J-H, Wang A-L, Li G-R, Wang J-W, Ou Y-N and Tong Y-X 2012 $Co_3O_4/Ni(OH)_2$ Composite Mesoporous Nanosheet Networks as a Promising Electrode for Supercapacitor Applications *J. Mater. Chem.* **22** 5656-65
[39] Wang G X, Chen Y, Konstantinov K, Yao J, Ahn J-h, Liu H K and Dou S X 2002 Nanosize Cobalt Oxides as Anode Materials for Lithium-ion Batteries *J. Alloys Compd.* **340** L5-L10
[40] Yang X, Fan K, Zhu Y, Shen J, Jiang X, Zhao P, Luan S and Li C 2013 Electric Papers of Graphene-Coated Co_3O_4 Fibers for High-Performance Lithium-Ion Batteries *ACS Appl. Mater. Interfaces* **5** 997-1002
[41] Kang Y-M, Song M-S, Kim J-H, Kim H-S, Park M-S, Lee J-Y, Liu H K and Dou S X 2005 A Study on the Charge-Discharge Mechanism of Co_3O_4 as an Anode for the Li ion Secondary Battery *Electrochim. Acta* **50** 3667-73
[42] Li W Y, Xu L N and Chen J 2005 Co_3O_4 Nanomaterials in Lithium-Ion Batteries and Gas Sensors *Adv. Func. Mater.* **15** 851-7
[43] Zhao Z W, Guo Z P and Liu H K 2005 Non-Aqueous Synthesis of Crystalline Co_3O_4 Powders Using Alcohol and Cobalt Chloride as a Versatile Reaction System for Controllable Morphology *J. Power Sources* **147** 264-8
[44] Li X, Dhanabalan A and Wang C 2011 Enhanced Electrochemical Performance of Porous NiO–Ni Nanocomposite Anode for Lithium Ion Batteries *J. Power Sources* **196** 9625-30
[45] Poizot P, Laruelle S, Grugeon S, Dupont L and Tarascon J M 2000 Nano-Sized Transition-Metal Oxides as Negative-Electrode Materials for Lithium-ion Batteries *Nature* **407** 496-9

[46] Varghese B, Reddy M V, Yanwu Z, Lit C S, Hoong T C, Subba Rao G V, Chowdari B V R, Wee A T S, Lim C T and Sow C-H 2008 Fabrication of NiO Nanowall Electrodes for High Performance Lithium Ion Battery *Chem. Mater.* **20** 3360-7
[47] Li J, Xiong S, Liu Y, Ju Z and Qian Y 2013 High Electrochemical Performance of Monodisperse $NiCo_2O_4$ Mesoporous Microspheres as an Anode Material for Li-Ion Batteries *ACS Appl. Mater. Interfaces* **5** 981-8
[48] Li F, Zou Q-Q and Xia Y-Y 2008 CoO-Loaded Graphitable Carbon Hollow Spheres as Anode Materials for Lithium-ion Battery *J. Power Sources* **177** 546-52
[49] Wang G X, Chen Y, Konstantinov K, Lindsay M, Liu H K and Dou S X 2002 Investigation of Cobalt Oxides as Anode Materials for Li-ion Batteries *J. Power Sources* **109** 142-7
[50] Swider-Lyons K E, Love C T and Rolison D R 2002 Improved Lithium Capacity of Defective V_2O_5 Materials *Solid State Ion.* **152–153** 99-104
[51] Li L, Cheah Y, Ko Y, Teh P, Wee G, Wong C, Peng S and Srinivasan M 2013 The Facile Synthesis of Hierarchical Porous Flower-like $NiCo_2O_4$ with Superior Lithium Storage Properties *J. Mater. Chem. A* **1** 10935-41
[52] Li B, Cao H, Shao J, Li G, Qu M and Yin G 2011 Co3O4@graphene Composites as Anode Materials for High-Performance Lithium Ion Batteries *Inorg. Chem.* **50** 1628-32
[53] Yoo E, Kim J, Hosono E, Zhou H-s, Kudo T and Honma I 2008 Large Reversible Li Storage of Graphene Nanosheet Families for Use in Rechargeable Lithium Ion Batteries *Nano Lett.* **8** 2277-82
[54] Hadjiev V G, Iliev M N and Vergilov I V 1988 The Raman spectra of Co_3O_4 *J. Phys. C* **21** L199-L201
[55] Choi H C, Jung Y M, Noda I and Kim S B 2003 A Study of the Mechanism of the Electrochemical Reaction of Lithium with CoO by Two-Dimensional Soft X-ray Absorption Spectroscopy (2D XAS), 2D Raman, and 2D Heterospectral XAS − Raman Correlation Analysis *J. Phys. Chem. B* **107** 5806-11
[56] Liu H-C and Yen S-K 2007 Characterization of Electrolytic Co_3O_4 Thin Films as Anodes for Lithium-ion Batteries *J. Power Sources* **166** 478-84
[57] Choi H C, Jung Y M and Kim S B 2005 Size Effects in the Raman Spectra of TiO_2 Nanoparticles *Vib. Spectrosc.* **37** 33-8